

Article

Structure, Corrosion Resistance, Mechanical and Tribological Properties of ZrB₂ and Zr-B-N Coatings

Philipp Kiryukhantsev-Korneev ^{*}, Alina Sytchenko , Yuriy Kaplanskii, Alexander Sheveyko, Stepan Vorotilo and Evgeny Levashov 

Scientific-Educational Center of SHS, National University of Science and Technology “MISIS”, 119049 Moscow, Russia; alina-sytchenko@yandex.ru (A.S.); ykaplansky@mail.ru (Y.K.); sheveyko@mail.ru (A.S.); stepan.vorotylo@gmail.com (S.V.); levashov@shs.misis.ru (E.L.)

* Correspondence: kiruhantsev-korneev@yandex.ru; Tel.: +7-(495)-638-46-59

Abstract: The coatings ZrB₂ and Zr-B-N were deposited by magnetron sputtering of ZrB₂ target in Ar and Ar–15%N₂ atmospheres. The structure and properties of the coatings were investigated via scanning and transmission electron microscopy, energy dispersion analysis, optical profilometry, glowing discharge optical emission spectroscopy and X-ray diffraction analysis. Mechanical and tribological properties of the coatings were investigated using nanoindentation, “pin-on-disc” tribological testing and “ball-on-plate” impact testing. Free corrosion potential and corrosion current density were measured by electrochemical testing in 1 N H₂SO₄ and 3.5%NaCl solutions. The oxidation resistance of the coatings was investigated in the 600–800 °C temperature interval. The coatings deposited in Ar contained 4–11 nm grains of the h-ZrB₂ phase along with free boron. Nitrogen-containing coatings consisted of finer crystals (1–4 nm) of h-ZrB₂, separated by interlayers of amorphous a-BN. Both types of coatings featured hardness of 22–23 GPa; however, the introduction of nitrogen decreased the coating’s elastic modulus from 342 to 266 GPa and increased the elastic recovery from 62 to 72%, which enhanced the wear resistance of the coatings. N-doped coatings demonstrated a relatively low friction coefficient of 0.4 and a specific wear rate of $\sim 1.3 \times 10^{-6} \text{ mm}^3\text{N}^{-1}\text{m}^{-1}$. Electrochemical investigations revealed that the introduction of nitrogen into the coatings resulted in the decrease of corrosion current density in 3.5% NaCl and 1 N H₂SO₄ solution up to 3.5 and 5 times, correspondingly. The superior corrosion resistance of Zr-B-N coatings was related to the finer grains size and increased volume of the BN phase. The samples ZrB₂ and Zr-B-N resisted oxidation at 600 °C. N-free coatings resisted oxidation (up to 800 °C) and the diffusion of metallic elements from the substrate better. In contrast, Zr-B-N coatings experienced total oxidation and formed loose oxide layers, which could be easily removed from the substrate.



Citation: Kiryukhantsev-Korneev, P.; Sytchenko, A.; Kaplanskii, Y.; Sheveyko, A.; Vorotilo, S.; Levashov, E. Structure, Corrosion Resistance, Mechanical and Tribological Properties of ZrB₂ and Zr-B-N Coatings. *Metals* **2021**, *11*, 1194. <https://doi.org/10.3390/met11081194>

Academic Editor: Frank Czerwinski

Received: 29 June 2021

Accepted: 22 July 2021

Published: 27 July 2021

Publisher’s Note: MDPI stays neutral with regard to jurisdictional claims in published maps and institutional affiliations.



Copyright: © 2021 by the authors. Licensee MDPI, Basel, Switzerland. This article is an open access article distributed under the terms and conditions of the Creative Commons Attribution (CC BY) license (<https://creativecommons.org/licenses/by/4.0/>).

Keywords: magnetron sputtering; coating; ZrB₂; Zr-B-N; structure; mechanical and tribological properties; corrosion and oxidation resistance

1. Introduction

The borides of transitional metals are prospective candidates for protective coatings for machining tools [1], heavy-duty friction couplings [2], fuel cells [3], aerospace vehicles [4], etc., due to the inherent high hardness, resistance towards corrosion, high-temperature oxidation and wear, high diffusion-barrier properties and low friction coefficient. The recent two decades saw considerable research efforts dedicated to coatings in Ta-B [5,6], V-B [7], Ti-B [1,8,9], Hf-B [10], W-B [11] and Ru-B [12] systems.

The introduction of nitrogen in the composition of the boride coatings opens the opportunity for the formation of nanocomposite structure comprised of nanosized crystals of borides or nitrides of transitional metals and amorphous boron nitride-based interlayers. Such structures display a unique combination of hardness up to 40 GPa, 70–90% elastic recovery, phase stability and oxidation resistance up to 900–1000 °C [13]. The introduction

of nitrogen can significantly alter the tribological properties and corrosion resistance of the coatings due to the formation of additional amorphous phases and grain refinement [14]. Previous works dedicated to coatings Ti-B-N [15], Hf-B-N [16] and V-B-N [17] demonstrated that the engineering of the structure, mechanical performance and wear resistance can be achieved by variation of the nitrogen content in the coatings (primarily by the application of different sputtering atmospheres). In addition to academic research, multiple enterprises introduce new grades of boronitride coatings for the machining tools [18].

From the industrial point of view, ZrB₂ and Zr-B-N-based coatings are prospective candidates for application due to their hardness of 22–29 GPa [19,20], high adhesion (critical stress of 80 N) [20]. ZrB₂-based coatings can be produced by a wide variety of techniques, including plasma deposition [21–23], diffusion saturation [24], salt electrolysis [25], electrospark deposition [26,27], chemical vapor deposition [28] and arc-PVD [29]. Magnetron sputtering offers several advantages, including low surface roughness, substrate geometry retention [30,31], low content of pores and structural defects [32,33], high adhesion to the substrate when the preliminary ion etching is applied [34–36], precise control of the structural characteristics via the adjustment of the sputtering parameters [37], the versatility of the used substrates [38–41] and uniform depth-wise distribution of the elements in the multi-element coatings [41–43].

This work aimed to conduct a comparative study of the structure, mechanical properties, tribological performance and corrosion resistance in aggressive gaseous and liquid media for two types of coatings deposited in Ar and Ar + 15%N₂ atmosphere by magnetron sputtering of a ZrB₂ target.

2. Materials and Methods

ZrB₂ sputtering targets with a diameter of 120 mm and height of 5 mm were produced by self-propagating high-temperature synthesis from the mixture of elemental boron and zirconium powders [44]. Magnetron sputtering of the targets was performed in DC mode using power unit Pinnacle Plus 5 × 5 (Advanced Energy), equipped with the arc extinguisher and able to automatically maintain the deposition parameters. The amperage and voltage of the current were 2 A and 400–500 V, correspondingly. The sputtering was performed in Ar and Ar + 15%N₂ atmospheres at 0.1–0.2 Pa pressure. As the substrates, we employed discs made of hard alloy VK6M (WC–6%Co), nickel alloy HN65VMTYu (international analog-Inconel C-276), aluminum oxide VOK-100-1 (sputtering duration 40 min) and KEF-4.5 grade monocrystalline silicon wafers (sputtering duration 15 min). Before coating deposition, the substrates were cleaned by ion etching (Ar⁺ ions with energy of 1.5–2 keV during 10 min) using a slot-type ion source. During the coating deposition, the temperature of the substrate did not exceed 300 °C.

To record the depth-wise elemental profiles and analysis of the chemical composition of the coatings we used glow-discharge optical emission spectroscopy [45] PROFILER-2 (Horiba Jobin Yvon, Longjumeau, France). Transverse fractures of the coatings were investigated using scanning electron microscope (SEM) S3400 (Hitachi, Tokyo, Japan) in the secondary electron mode (accelerating voltage 20–30 kV). X-ray diffraction analysis was carried out using Bragg-Brentano geometry as well as grazing incidence angle of 5° on a Bruker D8 diffractometer with monochromatic CuK α radiation. The phase composition of the coatings was additionally investigated using Raman spectroscopy Ntegra NT-MDT equipped with a 633 nm laser. High-resolution Transmission electron microscopy (HRTEM) investigations were performed using the coatings deposited on silicon wafers on the JEM-2100 (Jeol, Tokyo, Japan) microscope. To ascertain the mechanical performance of the coatings, we used Nano-Hardness Tester (CSM Instruments, Peseux, Switzerland). The penetration depth did not exceed 10% at the 4 mN load. Tribological testing was performed using Tribometer installation (CSM Instruments, Peseux, Switzerland) with a “pin-on-disk” scheme (5 N load), equipped with WC–6%Co ball (d = 3 mm). The wear tracks were investigated using optical profilometer Wyko-1100NT (Veeco, Plainview, NY, USA).

Cyclic impact testing of the coatings was performed on impact tester (CemeCon, Würselen, Germany) at 1000 N load for 10^5 cycles using a 5 mm WC-Co ball.

To ascertain the resistance of the coatings against high-temperature corrosion in air and diffusion of the substrate elements, we conducted stepwise annealing in SNOL-7.2/1200 furnace (AB “UMEGA”, Utena, Lithuania) at 600 and 800 °C with 1 h isothermal dwelling. After each annealing run, the depth-wise elemental profile was measured.

Electrochemical investigation of the coatings and substrate were performed using the three-electrode cell with potentiostat “Voltalab PST050” (Radiometer Analytical SAS, Lyon, France) (solutions 1 N H₂SO₄ and 3.5% NaCl, T = 25 °C). For statistics, 2 series of samples were examined. All potentials were normalized against standard hydrogen electrodes. Corrosion currents were calculated using the graphical representation of the Tafel equation.

3. Results and Discussion

According to the GDOES data, all elements were distributed uniformly across the depth of the coatings (Figure 1).

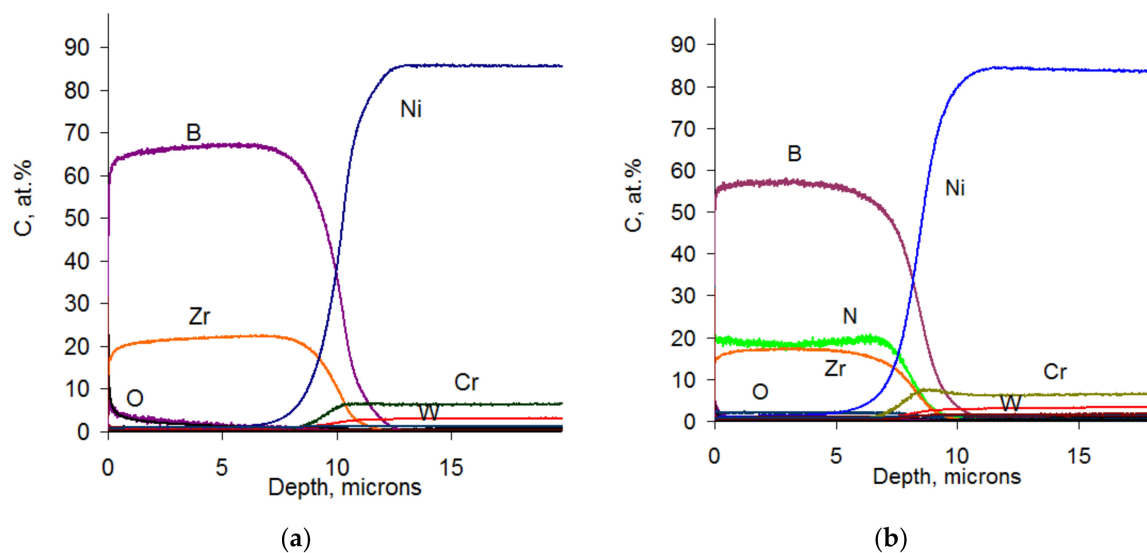


Figure 1. GDOES profiles for the coatings 1 (100%Ar) (a) and 2 (85%Ar + 15%N₂) (b).

The concentration of admixtures of carbon and oxygen did not exceed 1.5 at.% per element. The presence of the admixtures in the coatings can be attributed to the trace amounts of carbon and oxygen both in the sputtered target and in the sputtering atmosphere. The depth-averaged concentration of the main constituent elements is presented in Table 1.

Table 1. Composition, mechanical properties and tribological performance of the coatings.

№	Atmosphere	Composition, at.%			Mechanical Properties					f	Vw, × 10 ⁻⁶ mm ³ N ⁻¹ m ⁻¹
		Zr	B	N	H, ГПа	E, ГПа	H/E	H ³ /E ² , ГПа	W, %		
1	100%Ar	24 ± 2	76 ± 2	-	22	342	0.064	0.091	62	0.9	8.2
2	85%Ar + 15%N ₂	18 ± 2	61 ± 2	21 ± 2	23	266	0.086	0.172	72	0.4	1.3

The sputtering of ZrB₂ in Ar yielded coatings with 24 at.% Zr and 76 at.% B. This corresponds to the B/Zr ratio of 3.2 which is far from the stoichiometry of the target. The concentration of Zr and B predictably decreases to 18 and 61 at.% correspondingly (B/Zr = 3.4) upon the introduction of nitrogen in the sputtering atmosphere. The nitrogen content in N-doped coatings was approx. 21 at.%.

The SEM images of the morphology of the coatings are presented in Figure 2.

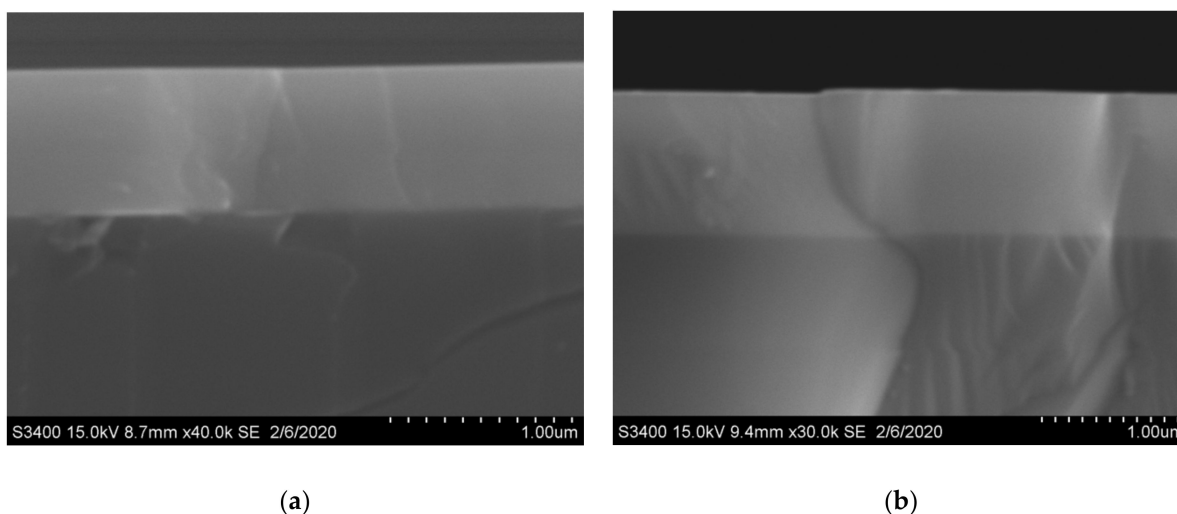


Figure 2. SEM images of the transverse fractures of the coatings 1 (100%Ar) (a) and 2 (85%Ar + 15%N₂) (b).

The analysis of the SEM images of the transverse fractures of the coatings deposited on silicon wafers suggests that all investigated coatings have a dense, defect-free structure. Both ZrB₂ and Zr-B-N coatings have a higher density as compared to the industry-standard two-component coatings [46,47]. The SEM-derived growth rate of the coatings was 52 and 49 nm/min in case of deposition in Ar and Ar + N₂, correspondingly.

According to XRD analysis, the only crystalline constituent of coating 1 is the ZrB₂ phase with hexagonal lattice (JCPDS 89–3930). XRD patterns show pronounced reflexes (001), (100), (101), (002) and (102) of h-ZrB₂ (Figure 3).

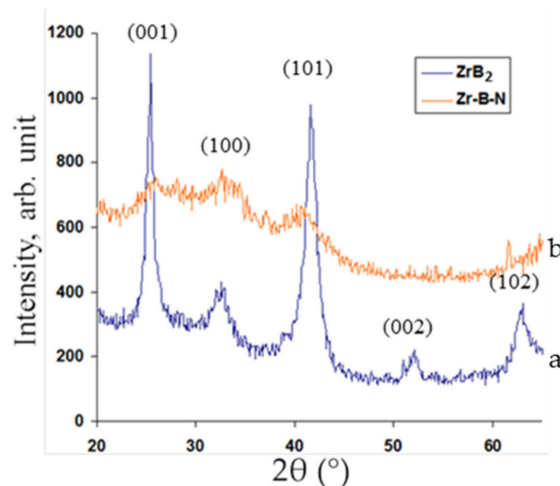


Figure 3. XRD patterns of coatings 1 (100%Ar) (a) and 2 (85%Ar + 15%N₂) (b).

This phase is characterized by a pronounced texture in (001) direction, which coincides with the coating's growth direction. Mean crystallite size was calculated using half-width of (001), (100) and (101) lines and was equal to 6–11 nm. The introduction of nitrogen decreased the size of h-ZrB₂ crystallites to 1–2 nm and changed the preferential orientation to (100). Similar trends were observed previously for the coatings based on borides of Cr and Ti [13]. The lattice spacings calculated using the three most intense lines on XRD patterns for the coatings deposited in Ar were 0.359, 0.292 and 0.232 nm. It should be noted that according to the reference data, the spacings for h-ZrB₂ are 0.353, 0.274, 0.216 nm. Therefore, we report results that are close or slightly higher as compared to the reference, which might be related to the introduction of excess boron atoms into the interstitial positions of the ZrB₂ lattice [48]. Additionally, internal stresses in the coatings can also

affect the position of the diffraction lines [49]. For the N-doped coatings, the following spacings were obtained: 0.351, 0.282 and 0.236 nm. A minor reduction of the interplanar spacings in coating 2 as compared to coating 1 might be related to the precipitation of excess boron from h-ZrB₂ and the formation of an amorphous boron-based phase.

According to the XRD data, coating 1 contained a single crystalline phase h-ZrB₂. The introduction of 21%N into ZrB₂ coatings did not result in the formation of any nitrogen-containing crystalline phases. Since the atomic ratio B/Zr = 3.2–3.4, both coatings 1 and 2 contain excess boron. Therefore, one might expect the formation of amorphous structural constituents, which cannot be traced by XRD (such as B and BN). Raman spectroscopy of coating 1 demonstrated the presence of ZrB₂ (peak at 514 cm⁻¹) [50], as well as free boron (intensely widened peak at ~800 cm⁻¹) [51]. Coating 2 in addition to the peak at 515 cm⁻¹ shows peaks at 1343 and 1535 cm⁻¹, which are characteristic of the BN phase [52,53] (Figure 4).

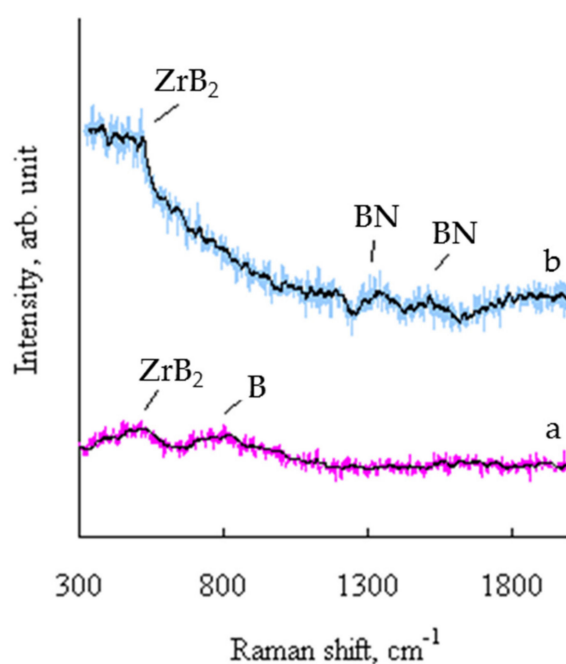


Figure 4. Raman spectra of the coatings 1 (100%Ar) (a) and 2 (85%Ar + 15%N₂) (b).

TEM images of the microstructures and SAED patterns of the coatings 1 and 2 are presented in Figure 5.

The lamellas for TEM were prepared using a standard technique, which includes gluing, mechanical thinning and ion etching. This approach allowed us to analyze the transverse cross-section of the coatings. The TEM images of both reactive and non-reactive coatings feature equiaxial microstructures. Usually, ZrB₂ coatings are characterized by columnar microstructure [54,55]. The absence of the columnar microstructure in the case of ZrB₂ coating (coating 1) can be attributed to the accumulation of strain in the crystalline structure of ZrB₂ due to the oversaturation by boron atoms, premature inhibition of the grain growth and formation of the additional B-B phase, which suppresses the layer-by-layer growth of the columnar structures.

The SAED patterns (Figure 5a) of coating 1 shows prominent reflexes from h-ZrB₂. Interplanar spacings calculated using SAED were 0.330, 0.265 and 0.210 nm. The TEM-derived grains size of the h-ZrB₂ phase in coating 1 was 4–11 nm, which correlates well with the XRD-derived results. The TEM-derived interplanar spacings for coating 1 were 0.361, 0.289 and 0.226 nm, which corresponds well with the XRD data.

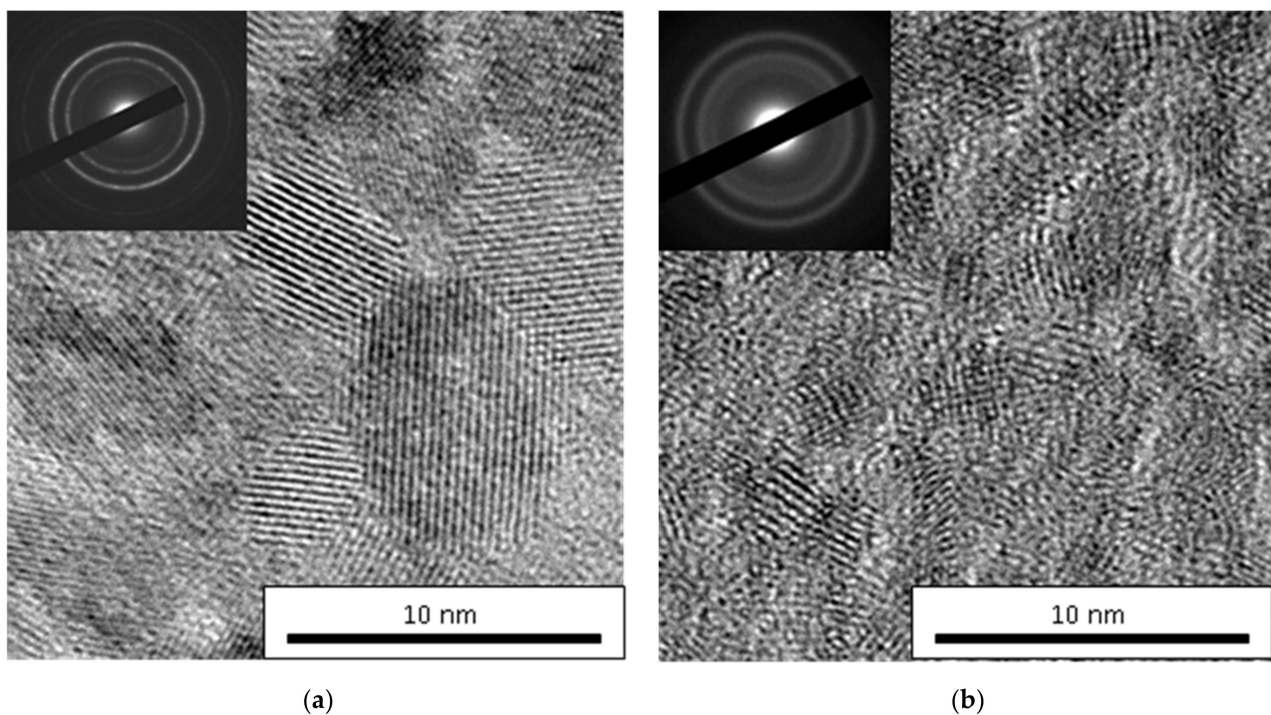


Figure 5. HR TEM images and SAED patterns of coatings 1 (100%Ar) (a) and 2 (85%Ar + 15%N₂) (b).

The SAED patterns of coating 2 show significantly broadened lines; however, the interplanar spacings (d-spacings) measured from the location of the center of each line were close to that of coating 1 and were equal to 0.325, 0.269 and 0.209 nm, which corroborates the presence of h-ZrB₂ phase. The introduction of nitrogen decreases the grain size of the crystalline phase to 1.5–3.5 nm and the formation of prominent 1–2 nm wide amorphous interlayers (Figure 5b). A similar effect of grain refinement was previously reported [56,57]. According to the TEM data for coating 2, the reflexes have interplanar spacings of 0.238 and 0.250 nm, which can correspond both to the ZrB₂ and cubic ZrN, i.e., we cannot exclude the possibility of ZrN formation. The volume ratio of such crystallites was approx. 7%.

The results of the mechanical testing of the coatings deposited on hard alloy VK6M substrate are shown in Table 1. Both coatings 1 and 2 demonstrated close hardness values (H = 22–23 GPa). Upon the introduction of nitrogen, the elastic modulus (E) decreased by 22% and the elastic recovery (W) increased by 16%. This effect can be related to a variety of factors, such as changes in the internal stresses and coating's texture, grain refinement and emergence of new N-containing phases. The higher values of elastic recovery W = 72%, as well as plasticity index H/E = 0.086 and resistance to plastic deformation H³/E² = 0.172 GPa were attained for the Zr-B-N coatings. The elastic-plastic characteristics W, H/E and H³/E² can significantly affect the fracture toughness, wear-resistance and tribological performance of the investigated coatings [58–60].

Experiments demonstrated that nitrogen-free Zr-B coatings display a higher friction coefficient as compared to reactive N-doped coatings. In the first case, during the 0–10 m distance, the friction coefficient reaches 0.8–0.9 and occasionally rises to 1.1 (Figure 6a).

Afterward, the friction coefficient decreases to 0.6 and then rises again and stabilizes at 0.9. The oscillations of the friction coefficient in such a broad interval are caused by rapid degradation and wear of the N-free coating (complete wear at 100 m). In the case of N-doped coatings, after the first running-in time (less than 5 m) the friction coefficient stabilizes and remains constant (0.44) during the rest of the tribological test. This stark difference is caused by the presence of an amorphous phase (a-BN) in N-doped coatings, which upon tribo contact easily reacts with the oxygen from air with the formation of B₂O₃ and then reacts with the water vapor (air humidity was 40–50%) with the formation of boric acid H₃BO₃. This acid possesses layered structures and acts as a solid lubricant

during tribological testing [61]. Additionally, the higher fracture toughness of the N-doped coatings can also play a role [36,62].

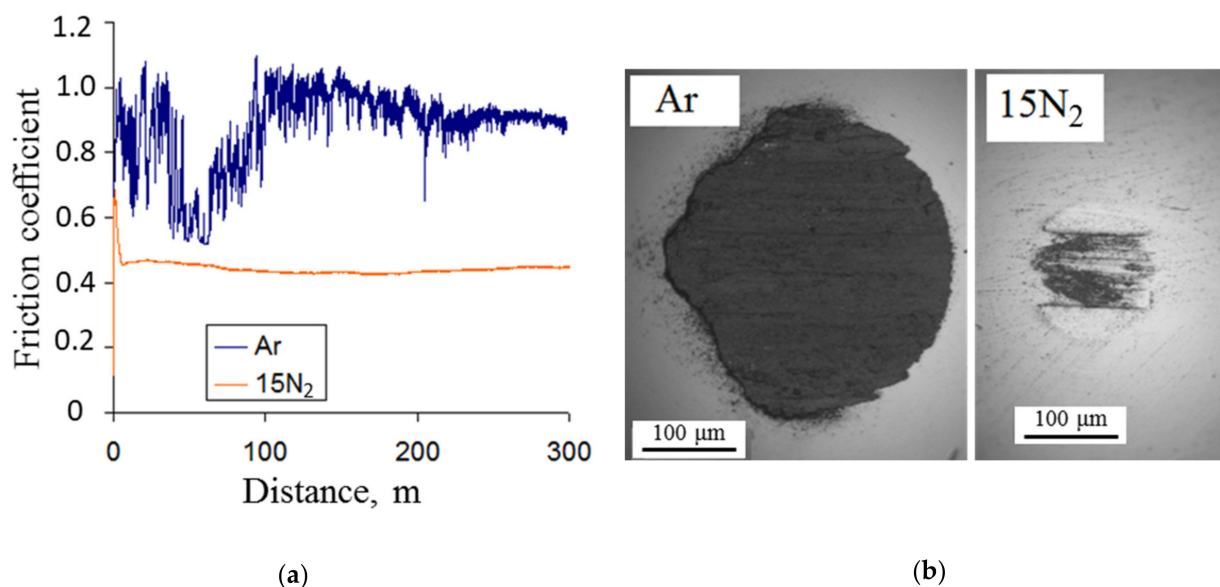


Figure 6. Dependence of the friction coefficient on the distance (a) and photo of the wear zones of the counter-bodies (b).

The reduction of friction coefficient in the N-doped coatings leads to a substantial decrease in the wear of the counter-body (Figure 6b): the diameter of the worn-out area decreases from 350 to 150 μm. The N-free coatings experience rapid and complete wear and the wear track has areas of brittle fracture, in which the depth of the wear track is ≥ 3.5 μm, i.e., is deeper than the coating itself (Figure 7). The width of the wear track in these locations is 70–100 μm. In other areas, the wear track depth was 500–700 nm at 50–200 μm track width. In the coatings with the highest nitrogen content, the wear track has a uniform perimeter. The depth of the wear track is below 1 μm, with a width of 90–100 μm. The profiles of the wear tracks were used to calculate the specific wear rate of the coatings (Table 2). The lower specific wear rate of $1.3 \times 10^{-6} \text{ mm}^3\text{N}^{-1}\text{m}^{-1}$ was obtained for the reactive Zr-B-N coatings. For the binary boride coatings, the wear rate was almost an order of magnitude higher— $8.2 \times 10^{-6} \text{ mm}^3\text{N}^{-1}\text{m}^{-1}$. Thus, the N-doped coatings possessed higher wear resistance as a result of their higher mechanical properties (W , H/E , H^3/E^2) [63]. Analysis of published literature demonstrated that the coatings Zr-B-N, produced by magnetron sputtering, in case of sliding friction against Al_2O_3 counter-body were characterized by a high friction coefficient of 0.69–0.75 and specific wear rate of $1.8\text{--}2.8 \times 10^{-6} \text{ mm}^3\text{N}^{-1}\text{m}^{-1}$ [54].

N-free coatings demonstrated higher resistance towards dynamic loads: the depth of wear holes was ~ 7 μm, with 550 μm diameter (Figure 8).

Uniform wear across the area of the tribological contact was observed. In the case of N-doped coatings, the surface layer experienced rapid degradation, followed by wear of the surface (exacerbated by the presence of products of coating's wear). The wear hole was non-uniform, with a max depth of 13 μm and diameter of 750 μm. Therefore, the introduction of nitrogen decreases the impact resistance of the coatings. This effect can be attributed to the higher elastic modulus of ZrB_2 coatings, which is close to the values for the substrate ($E = 450\text{--}500$ GPa) [64].

The results of electrochemical testing of coatings and uncoated substrate VK6M (WC–6%Co) in water solutions of 3.5% NaCl and 1 N H_2SO_4 are demonstrated in Figure 9 as polarization curves in semi-logarithmic coordinates. The free corrosion potential E and corrosion current density I_{corr} are provided in Table 2.

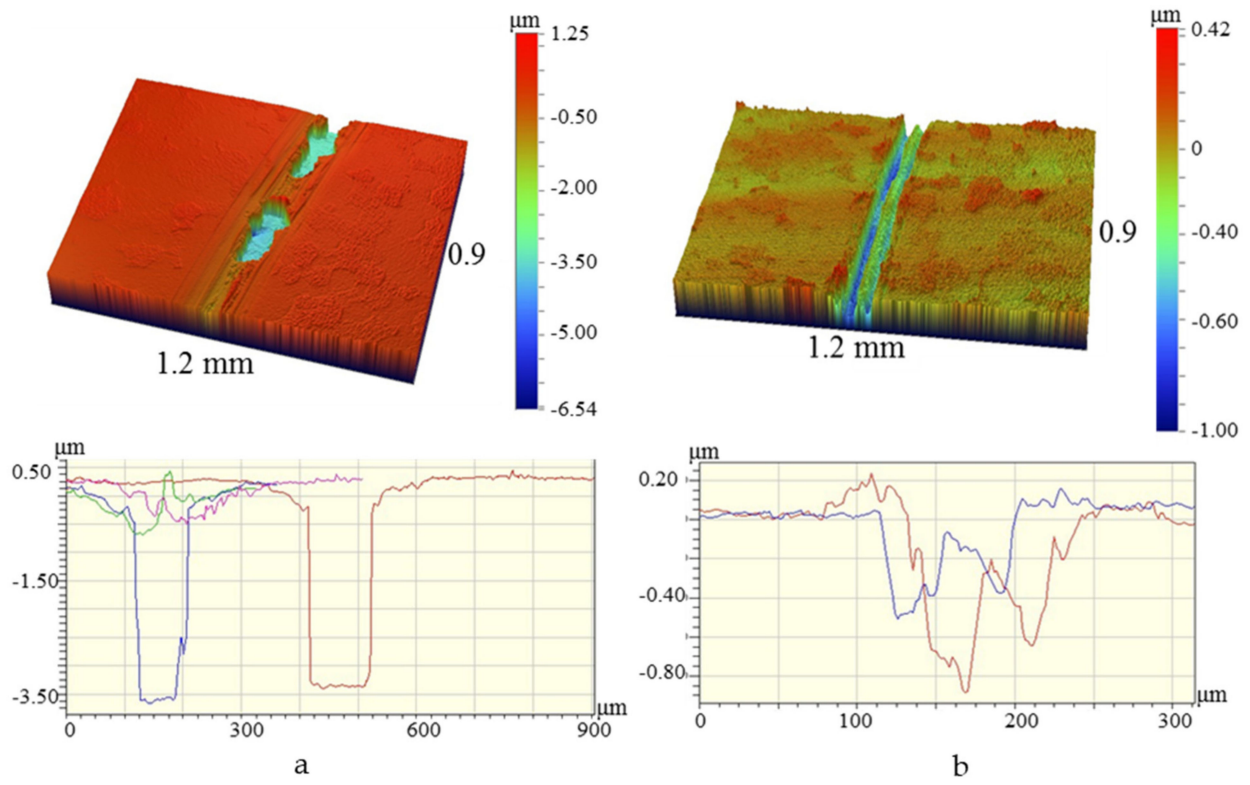


Figure 7. 3D and 2D profiles of the wear tracks for coatings 1 (100%Ar) (a) and 2 (85%Ar + 15%N₂) (b).

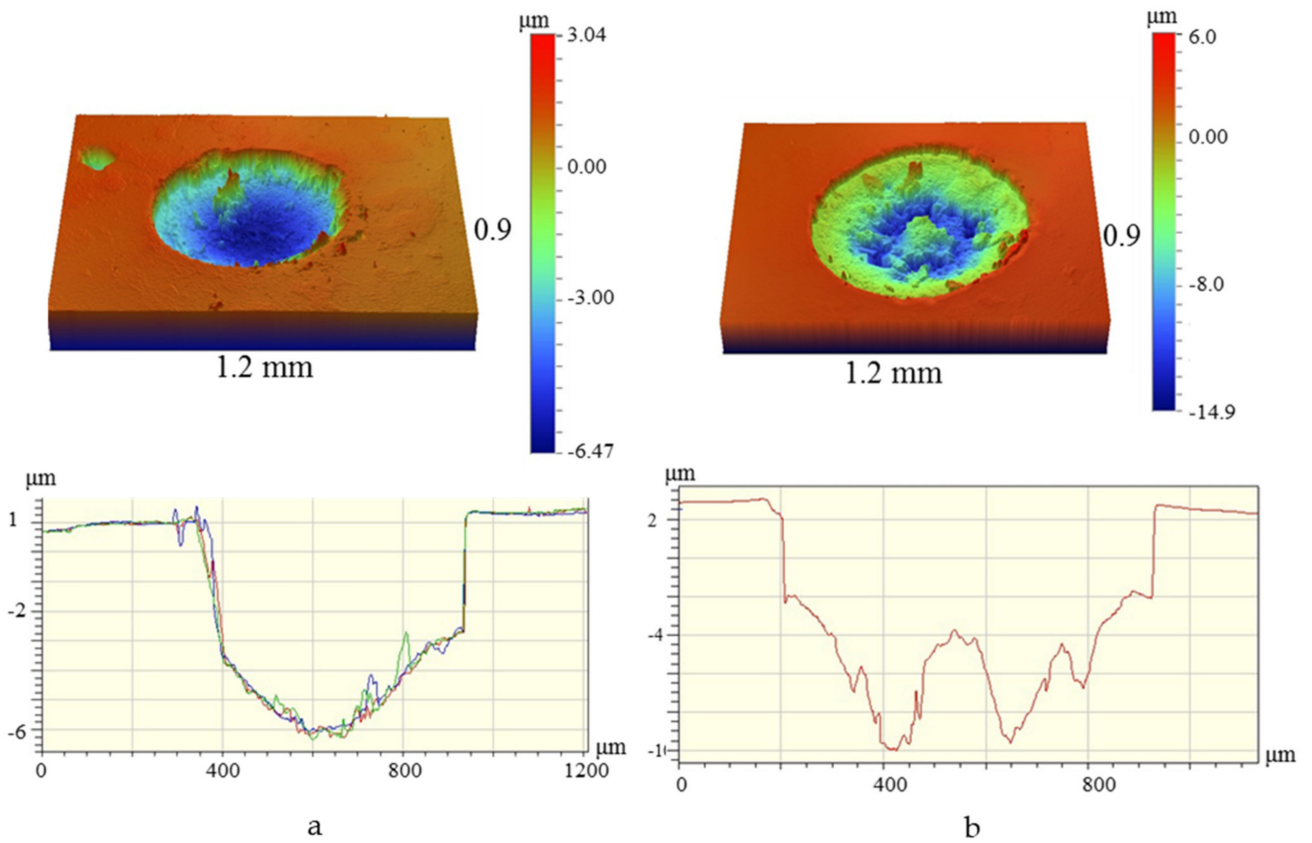


Figure 8. 3D and 2D profiles of wear holes for the coatings 1 (100%Ar) (a) and 2 (85%Ar + 15%N₂) (b).

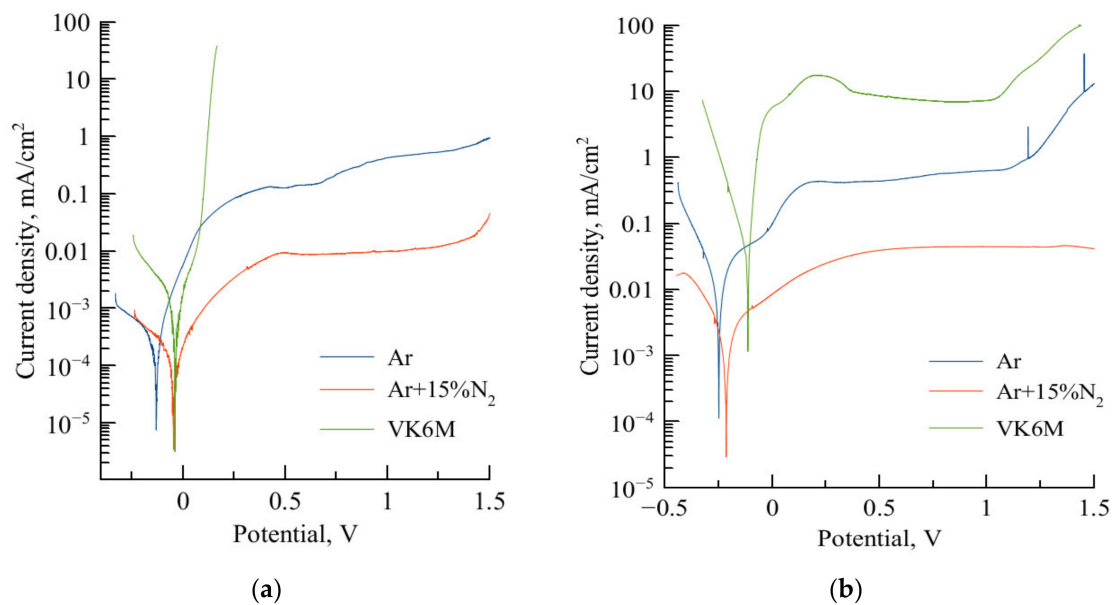


Figure 9. Results of electrochemical testing in 3.5% NaCl (a) and 1 N H₂SO₄ (b) solutions.

Table 2. The results of electrochemical investigations.

Sample	Atmosphere	3.5% NaCl		1 N H ₂ SO ₄	
		<i>E</i> , mV	<i>I</i> _{corr} , μA/cm ²	<i>E</i> , mV	<i>I</i> _{corr} , μA/cm ²
1	Ar	−131	0.24	−250	8.7
2	Ar + 15%N ₂	−47	0.07	−216	1.7
	Substrate WC−6%Co	−39	1.15	−115	33.0

In a 3.5% NaCl, both coatings demonstrated stable passivated behavior. Upon anode polarization, both coatings 1 and 2 showed passive behavior up to the potential of 1.5 V. Hard-alloy substrate experienced rapid corrosion, which can be seen from the value of corrosion current density and the rapid rise of current upon anode polarization. The settled free corrosion potentials for coatings 1, 2 and uncoated substrate were −131, −47 and −39 mV, correspondingly. The comparison of the corrosion currents (Table 2) revealed that the introduction of nitrogen in the composition of the coatings decreased the current density by 3.5 times. A similar effect was observed in [65]. One should note that the coatings ZrB₂ and Zr-B-N showed an order of magnitude higher corrosion resistance in 3.5% NaCl as compared to the hard alloy.

Electrochemical testing of the coatings in 1 N H₂SO₄ (Figure 9b) demonstrated that the coating 1 and substrate are passivated up to 1 V. Beyond 1 V, the break-up of the passive film occurs, followed by dissolution of the material. The coating deposited in Ar + 15%N₂ atmosphere retains its passive state up to 1.5 V. The free corrosion potentials of the coatings 1, 2 and substrate in 1 N H₂SO₄ were −250, −216 and −115 mV, correspondingly. The corrosion current density decreased in the following sequence: VK6M substrate (33.0 μA/cm²) → non-reactive ZrB₂ coating (8.7 μA/cm²) → N-doped coating Zr-B-N (1.7 μA/cm²). The introduction of N in the composition of the coating resulted in a 5-fold decrease in the corrosion current density. One should note that coatings 1 and 2 increase the resistance of the hard alloy towards corrosion in 1 N H₂SO₄ by ~4 and 20 times, correspondingly. According to the literature data, coatings ZrB₂ and Zr-B-N, tested in similar 1 N H₂SO₄ solution, demonstrated corrosion current densities of 1.93 and 0.60 mA/cm² [65], which are substantially higher than the values obtained in our work.

Therefore, the best corrosion resistance in 3.5% NaCl and 1 N H₂SO₄ solutions were obtained for the coatings deposited in Ar + 15%N₂ atmospheres. The increase of the corro-

sion resistance upon the introduction of the nitrogen can be associated with the changes in the phase composition and formation of nanocomposite microstructure in the coatings [20]. According to our TEM and XRD data, the introduction of N into the ZrB_2 coatings resulted in the alteration of the microstructure of the coatings, namely the refinement of the grains size from 4–11 nm to 1–4 nm and an increase in the volume percentage of the amorphous phase. It is known that a dense and fine-grained microstructure of the coatings promotes the formation of stable passivated layers [66,67]. The differences in the corrosion resistance between coatings 1 and 2 can be attributed to the distinction in the conductivity of free boron and boron nitride [68,69]. An important factor for the improvement of the protective properties of the coatings is the continuity and width of the amorphous interlayers which surround ZrB_2 grains. In the case of Zr-B-N coatings, the ZrB_2 grains are separated by relatively thick interlayers of dielectric BN phase [70,71]. Since there is no definitive proof regarding the formation of the ZrN phase (or lack thereof), we conjecture that this corrosion-resistant phase can also enhance the coating's corrosion performance [72].

To ascertain the high-temperature oxidation resistance of the coatings, stepwise oxidation annealing runs were performed using coatings deposited on corrosion-resistant nickel-based alloy HN65VMTYu. Based on the GDOES-derived of depth-wise elemental profiles we calculated the thickness of the oxide layers on top of the tested coatings. Results for coating 1 are provided in Figure 10.

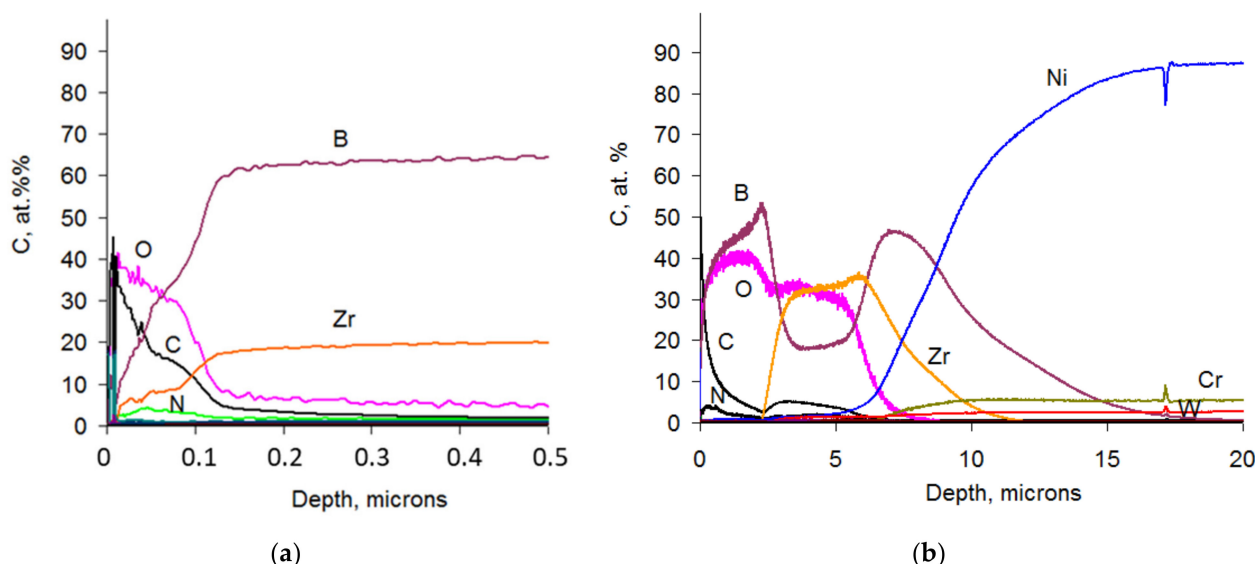


Figure 10. Depth-wise elemental profiles for coating 1 (100%Ar) after annealing in air at 600 °C (a) and 800 °C (b).

Both coatings 1 and 2 resisted oxidation at 600 °C. According to the GDOES data, the penetration depth of the oxygen atoms in coatings 1 and 2 was 120 and 90 nm, correspondingly. The composition of the upper layer was based on the zirconium dioxide with minor retention of boron. The main volume of boron apparently evaporated from the surface in form of the volatile oxide B_2O_3 [73,74]. Upon the increase of the temperature to 800 °C the coating 2 suffered complete oxidation and transformed into a porous oxide layer with poor strength and adhesion towards the substrate (the oxide layer was destroyed by a single measurement on spectrometer). The low oxidation resistance of the coatings in the Zr-B-N system is related to the formation of oxides of boron and nitrogen upon heating in air. These oxides have high saturated vapor pressure at 800 °C and therefore evaporate rapidly and compromise the structural integrity of the coatings [75,76]. The heating of N-free coating 1 up to 800 °C resulted in the formation of a 2–2.5 μm thick upper oxide layer based on boron oxide. Under this upper layer lies an intermediate 3 μm thick layer consisting of the mixture of ZrO_2 and B_2O_3 and an oxygen-free layer, which consists of Zr, B and a minor

amount of Ni from the substrate, underneath which lies the substrate itself (a nickel alloy based on Ni, Cr and W). The as-formed layered structure possessed high strength.

4. Conclusions

Using the magnetron sputtering of ceramic cathodes, which were fabricated by self-propagating high-temperature synthesis, we produced coatings ZrB₂ and Zr-B-N. The non-reactive coatings were based on the ZrB₂ phase with a hexagonal lattice, with a minor amount of amorphous boron. The introduction of nitrogen does not lead to the formation of additional crystalline phases but resulted in the decrease of the grains size from 4–11 to 1–4 nm and change from the texture orientation from (001) to (100) and formation of amorphous 1–2 nm thick grain boundary interlayers of amorphous a-BN phase.

The hardness of both N-free and N-doped coatings was equal to 22–23 GPa. However, N-doped coatings demonstrated a decrease in elastic modulus and an increase of elastic recovery by 20% and 16% as compared to the ZrB₂ coatings. Due to the higher fracture toughness, the Zr-B-N coating surpassed the non-reactive coating in terms of tribological performance and demonstrated a stable friction coefficient of 0.4 and a specific wear rate of $1.3 \times 10^{-6} \text{ mm}^3\text{N}^{-1}\text{m}^{-1}$.

Resistance towards gaseous corrosion of Zr-B-N coatings is based on the formation on the surface of the coating of a zirconia-based protective layer, which impedes the diffusion of oxygen into the coating. The increase in Zr content improves the oxidation resistance of the coatings, whereas the higher content of boron and nitrogen compromises the oxidation resistance due to the rapid formation and evaporation of BO_x and NO_x.

Electrochemical investigations in a 3.5% NaCl revealed that the coatings ZrB₂ and Zr-B-N have an order of magnitude higher corrosion resistance as compared to the hard alloy substrate. The introduction of nitrogen into the coating resulted in a 3.5-fold decrease in the corrosion current density. In the 1 N H₂SO₄ solution the corrosion current density decreased in the following sequence: WC–6%Co substrate (33.0 μA/cm²) → N-free ZrB₂ coating (8.7 μA/cm²) → N-doped coating Zr-B-N (1.7 μA/cm²). The introduction of nitrogen into the composition of the coating has led to a 5-fold decrease in the corrosion current density.

The increase of corrosion resistance in 3.5% NaCl and 1 N H₂SO₄ solutions upon the introduction of nitrogen into the coatings is related to the decrease of the size of h-ZrB₂ crystallites, change of the composition of amorphous interlayers from B-B to B-N and increase of the interlayers' thickness. The amorphous B-N interlayers with high electrical resistance, increased volume percentage and nanometric thickness, provide efficient isolation for the h-ZrB₂ crystallites and impede their corrosion.

Author Contributions: Supervision, conceptualization, deposition, annealing, GDOES investigation, writing and editing: P.K.-K.; formal analysis, electrochemical investigation, profilometry, calculations, writing: A.S. (Alina Sytchenko); translating, editing: S.V.; HR TEM investigation: Y.K., data curation: A.S. (Alexander Sheveyko); Resources: E.L. All authors have read and agreed to the published version of the manuscript.

Funding: This work was performed with financial support from Russian Foundation for Basic Research (project № 19-08-00187). HR TEM studies were supported by the Ministry of Science and Higher Education of the Russian Federation (project 0718-2020-0034 of State Assignment).

Institutional Review Board Statement: Not applicable.

Informed Consent Statement: Not applicable.

Data Availability Statement: The data presented in this study are available on request from the corresponding author.

Acknowledgments: The authors are grateful to N.V. Shvindina for her help in the SEM investigation, to M.I. Petzhik for his help with nanoindentation experiments and K. A. Kuptsov for his help with impact-testing.

Conflicts of Interest: The authors declare no conflict of interest.

References

1. Wallgram, W.; Schleinkofer, U. Synthesis, Structure, and Behavior of a new CVD TiB₂ Coatings with Extraordinary Properties for High Performance Applications. In Proceedings of the 17th Plansee Seminar, Reutte, Austria, 25–29 May 2009.
2. Taktak, S. Tribological behaviour of borided bearing steels at elevated temperatures. *Surf. Coat. Technol.* **2006**, *201*, 2230–2239. [[CrossRef](#)]
3. Hassan, H.B.; Abdel Hamid, Z. Electroless Ni-B supported on carbon for direct alcohol fuel cell applications. *Int. J. Hydrogen Energy* **2001**, *36*, 849–856. [[CrossRef](#)]
4. Li, H.; Yao, D.; Fu, Q.; Liu, L.; Zhang, Y.; Yao, X.; Wang, Y.; Li, H. Anti-oxidation and ablation properties of carbon/carbon composites infiltrated by hafnium boride. *Carbon* **2013**, *52*, 418–426. [[CrossRef](#)]
5. Ribeiro, R.; Ingole, S.; Usta, M.; Bindal, C.; Ucisik, A.H.; Liang, H. Tribological investigation of tantalum boride coating under dry and simulated body fluid conditions. *Wear* **2007**, *262*, 1380–1386. [[CrossRef](#)]
6. Goncharov, A.A.; Ignatenko, P.I.; Petukhov, V.V.; Konovalov, V.A.; Volkova, G.K.; Stupak, V.A.; Glazunova, V.A. Composition, structure, and properties of tantalum boride nanostructured films. *Tech. Phys.* **2006**, *51*, 1340–1343. [[CrossRef](#)]
7. Goncharov, A.A.; Petukhov, V.V.; Terpii, D.N.; Ignatenko, P.I.; Stupak, V.A. Nanostructured Films of Vanadium Borides. *Inorg. Mater.* **2005**, *41*, 696–699. [[CrossRef](#)]
8. Kunc, F.; Musil, J.; Mayrhofer, P.H.; Mitterer, C. Low-stress superhard Ti-B films prepared by magnetron sputtering. *Surf. Coat. Technol.* **2003**, *174–175*, 744–753. [[CrossRef](#)]
9. Ferrando, V.; Tarantini, C.; Manfrinetti, P.; Pallecchi, I.; Salvato, M.; Ferdeghini, C. Growth of diborides thin films on different substrates by pulsed laser ablation. *Thin Solid Films* **2006**, *515*, 1439–1444. [[CrossRef](#)]
10. Chatterjee, A.; Jayaraman, S.; Gerbi, J.E.; Kumar, N.; Abelson, J.R.; Bellon, P.; Polycarpou, A.A.; Chevalier, J.P. Tribological behavior of hafnium diboride thin films. *Surf. Coat. Technol.* **2006**, *201*, 4317–4322. [[CrossRef](#)]
11. Khor, K.A.; Yu, L.G.; Sundararajan, G. Formation of hard tungsten boride layer by spark plasma sintering boriding. *Thin Solid Films* **2005**, *478*, 232–237. [[CrossRef](#)]
12. Rau, J.V.; Latini, A.; Generosi, A.; Rossi Albertini, V.; Ferro, D.; Teghil, R.; Barinov, S.M. Deposition and characterization of superhard biphasic ruthenium boride films. *Acta Mater.* **2009**, *57*, 673–681. [[CrossRef](#)]
13. Kiryukhantsev-Korneev, F.V.; Novikov, A.V.; Sagalova, T.B.; Petrzhik, M.I.; Levashov, E.A.; Shtansky, D.V. A comparative study of microstructure, oxidation resistance, mechanical, and tribological properties of coatings in Mo-B-(N), Cr-B-(N) and Ti-B-(N) systems. *Phys. Met. Metallogr.* **2017**, *118*, 1136–1146. [[CrossRef](#)]
14. Levashov, E.A.; Shtansky, D.V.; Kiryukhantsev-Korneev, P.V.; Petrzhik, M.I.; Tyurina, M.Y.; Sheveiko, A.N. Multifunctional nanostructured coatings: Formation, structure, and the uniformity of measuring their mechanical and tribological properties. *Russ. Metall.* **2010**, 917–935. [[CrossRef](#)]
15. Holzschuh, H. Deposition of Ti-B-N (single and multilayer) and Zr-B-N coatings by chemical vapor deposition techniques on cutting tools. *Thin Solid Films* **2004**, *469*, 92–98. [[CrossRef](#)]
16. Jayaraman, S.; Gerbi, J.E.; Yang, Y.; Kim, D.Y.; Chatterjee, A.; Bellon, P.; Girolami, G.S.; Chevalier, J.P.; Abelson, J.R. HfB₂ and Hf-B-N hard coatings by chemical vapor deposition. *Surf. Coat. Technol.* **2006**, *200*, 6629–6633. [[CrossRef](#)]
17. Bazhin, A.I.; Goncharov, A.A.; Petukhov, V.V.; Radjabov, T.D.; Stupak, V.A.; Konovalov, V.A. Magnetron sputtering of a vanadium-diboride target in Ar+N₂ gaseous mixtures. *Vacuum* **2006**, *80*, 918–922. [[CrossRef](#)]
18. Holubar, P.; Jilek, M.; Sima, M. Present and possible future applications of superhard nanocomposite coatings. *Surf. Coat. Technol.* **2000**, *133*, 145–151. [[CrossRef](#)]
19. Mitterer, C.; Losbichler, P.; Werner, W.S.M.; Störi, H.; Barounig, J. Sputter deposition of decorative coatings based on ZrB₂ and ZrB₁₂. *Surf. Coat. Technol.* **1992**, *54*, 329–334. [[CrossRef](#)]
20. Wang, T.-G.; Liu, Y.; Zhang, T.; Kim, D.-I.; Kim, K.H. Influence of Nitrogen Flow Ratio on the Microstructure, Composition, and Mechanical Properties of DC Magnetron Sputtered Zr-B-O-N Films. *J. Mater. Sci. Technol.* **2012**, *28*, 981–991. [[CrossRef](#)]
21. Tului, M.; Ruffini, F.; Arezzo, F.; Lasisz, S.; Znamirovski, Z.; Pawlowski, L. Some properties of atmospheric air and inert gas high-pressure plasma sprayed ZrB₂ coatings. *Surf. Coat. Technol.* **2002**, *151*, 483–489. [[CrossRef](#)]
22. Zhong, W.; Niu, Y.; Hu, C.; Li, H.; Zeng, Y.; Zheng, X.; Ren, M.; Sun, J. High temperature oxidation resistance of metal silicide incorporated ZrB₂ composite coatings prepared by vacuum plasma spray. *Ceram. Int.* **2015**, *41*, 14868–14875. [[CrossRef](#)]
23. Xiang, Y.; Li, W.; Wang, S.; Chen, Z.-H.; Chen, H.-M. ZrB₂ coating for the oxidation protection of carbon fiber reinforced silicon carbide matrix composites. *Vacuum* **2013**, *96*, 63–68. [[CrossRef](#)]
24. Dong, Z.H.; Peng, X.; Wang, F.H. Oxidation of a ZrB₂ coating fabricated on Ta-W alloy by electrophoretic deposition and laser melting. *Mater. Lett.* **2015**, *148*, 76–78. [[CrossRef](#)]
25. Kaptay, C.; Kuznetsov, S.A. Electrochemical synthesis of refractory borides from molten salts. *Plasmas Ions* **1999**, *2*, 45–56. [[CrossRef](#)]
26. Verkhoturov, A.D.; Podchernyaeva, I.A.; Konevtsov, L.A. Spark alloying using metals and ZrB₂-based ceramics of tungsten-containing hard alloys for increasing serviceability. *Surf. Eng. Appl. Electrochem.* **2007**, *43*, 415–424. [[CrossRef](#)]
27. Verkhoturov, A.D.; Gordienko, P.S.; IPodchernyaeva, A.; Konevtsov, L.A.; Panin, E.S. The formation of protective coatings on tungsten-containing hard alloys by electrospark alloying with metals and borides. *Inorg. Mater. Appl. Res.* **2011**, *2*, 180–185. [[CrossRef](#)]

28. Sung, J.; Goedde, D.M.; Girolami, G.S.; Abelson, J.R. Remote-plasma chemical vapor deposition of conformal ZrB₂ films at low temperature: A promising diffusion barrier for ultralarge scale integrated electronics. *J. Appl. Phys.* **2002**, *91*, 3904–3911. [[CrossRef](#)]
29. Chapusot, V.; Pierson, J.F.; Lapostolle, F.; Billard, A. Arc-evaporated nanocomposite zirconium-based boronitride coatings. *Mater. Chem. Phys.* **2009**, *114*, 780–784. [[CrossRef](#)]
30. Ming'e, W.; Guojia, M.; Xing, L.; Chuang, D. Morphology and Mechanical Properties of TiN Coatings Prepared with Different PVD Methods. *Rare Met. Mater. Eng.* **2016**, *45*, 3080–3084. [[CrossRef](#)]
31. Chu, C.W.; Jang, J.S.C.; Chen, H.W.; Chuang, T.L. Enhanced wear resistance of the Cr-based thin film coating on micro drill by doping with W-C-N. *Thin Solid Films* **2009**, *517*, 5197–5201. [[CrossRef](#)]
32. Lawal, J.; Kiryukhantsev-Korneev, P.; Matthews, A.; Leyland, A. Mechanical properties and abrasive wear behaviour of Al-based PVD amorphous/nanostructured coatings. *Surf. Coat. Technol.* **2017**, *310*, 59–69. [[CrossRef](#)]
33. Kiryukhantsev-Korneev, F.V.; Sheveiko, A.N.; Komarov, V.A.; Blanter, M.S.; Skryleva, E.A.; Shirmanov, N.A.; Levashov, E.A.; Shtansky, D.V. Nanostructured Ti-Cr-B-N and Ti-Cr-Si-C-N coatings for hard-alloy cutting tools. *Russ. J. Non Ferrous Met.* **2011**, *52*, 311–318. [[CrossRef](#)]
34. Wu, J.; Wu, B.H.; Ma, D.L.; Xie, D.; Wu, Y.P.; Chen, C.Z.; Li, Y.T.; Sun, H.; Huang, N.; Leng, Y.X. Effects of magnetic field strength and deposition pressure on the properties of TiN films produced by high power pulsed magnetron sputtering (HPPMS). *Surf. Coat. Technol.* **2017**, *315*, 258–267. [[CrossRef](#)]
35. Kiryukhantsev-Korneev, P.V.; Sheveiko, A.N.; Petrzehik, M.I. Approaches to Increasing the Adhesion Strength of Hard Wear-Resistant Nanostructured Coatings Based on the Ti-B-(Cr, Si, C)-N System. *Prot. Met. Phys. Chem. Surf.* **2019**, *55*, 502–510. [[CrossRef](#)]
36. Kiryukhantsev-Korneev, P.V.; Pierson, J.F.; Bychkova, M.Y.; Manakova, O.S.; Levashov, E.A.; Shtansky, D.V. Comparative Study of Sliding, Scratching, and Impact-Loading Behavior of Hard CrB₂ and Cr-B-N Films. *Tribol. Lett.* **2016**, *63*, 44–55. [[CrossRef](#)]
37. Audronis, M.; Leyland, A.; Matthews, A.; Kiryukhantsev-Korneev, F.V.; Shtansky, D.V.; Levashov, E.A. The Structure and Mechanical Properties of Ti-Si-B Coatings Deposited by DC and Pulsed-DC Unbalanced Magnetron Sputtering. *Plasma Process. Polym.* **2007**, *4*, 687–692. [[CrossRef](#)]
38. Vančo, M.; Krmela, J.; Pešlová, F. The Use of PVD Coating on Natural Textile Fibers. *Procedia Eng.* **2016**, *136*, 341–345. [[CrossRef](#)]
39. Shtansky, D.V.; Grigoryan, A.S.; Toporkova, A.K.; Arkhipov, A.V.; Sheveiko, A.N.; Kiryukhantsev-Korneev, P.V. Modification of polytetrafluoroethylene implants by depositing TiCaPCON films with and without stem cells. *Surf. Coat. Technol.* **2011**, *206*, 1188–1195. [[CrossRef](#)]
40. Wenbin, F.; Mingjiang, D.; Chunbei, W.; Mingchun, Z.; Liang, H.; Huijun, H.; Songsheng, L. Magnetron Sputtering Preparation and Properties of SiC/MoSi₂ Oxidation Protective Coating for Carbon/Carbon Composites Prepared. *Rare Met. Mater. Eng.* **2016**, *45*, 2543–2548. [[CrossRef](#)]
41. Shtansky, D.V.; Kiryukhantsev-Korneev, P.V.; Bashkova, I.A.; Sheveiko, A.N.; Levashov, E.A. Multicomponent nanostructured films for various tribological applications. *Surf. Coat. Technol.* **2010**, *205*, 728–739. [[CrossRef](#)]
42. Tsai, D.-C.; Deng, M.-J.; Chang, Z.-C.; Kuo, B.-H.; Chen, E.-C.; Chang, S.-Y.; Shieu, F.-S. Oxidation resistance and characterization of (AlCrMoTaTi)-Si_x-N coating deposited via magnetron sputtering. *J. Alloys Compd.* **2015**, *647*, 179–188. [[CrossRef](#)]
43. Lin, C.H.; Duh, J.G.; Yeh, J.W. Multi-component nitride coatings derived from Ti-Al-Cr-Si-V target in RF magnetron sputter. *Surf. Coat. Technol.* **2007**, *201*, 6304–6308. [[CrossRef](#)]
44. Iatsyuk, I.V.; Lemesheva, M.V.; Kiryukhantsev-Korneev, P.V.; Levashov, E.A. Structure and properties of ZrB₂, ZrSiB and ZrAlSiB cathode materials and coatings obtained by their magnetron sputtering. In *IOP Conference Series: Materials Science and Engineering*; IOP Publishing: Bristol, UK, 2018; Volume 347, p. 012028. [[CrossRef](#)]
45. Kiryukhantsev-Korneev, F.V. Possibilities of glow discharge optical emission spectroscopy in the investigation of coatings. *Russ. J. Non Ferrous Met.* **2014**, *55*, 494–504. [[CrossRef](#)]
46. Polyakov, M.N.; Morstein, M.; Maeder, X.; Nelis, T.; Lundin, D.; Wehrs, J.; Best, J.P.; Edwards, T.E.J.; Döbeli, M.; Michler, J. Microstructure-driven strengthening of TiB₂ coatings deposited by pulsed magnetron sputtering. *Surf. Coat. Technol.* **2019**, *368*, 88–96. [[CrossRef](#)]
47. González-Carmona, J.M.; Triviño, J.D.; Gómez-Ovalle, Á.; Ortega, C.; Alvarado-Orozco, J.M.; Sánchez-Sthepa, H.; Avila, A. Wear mechanisms identification using Kelvin probe force microscopy in TiN, ZrN and TiN/ZrN hard ceramic multilayers coatings. *Ceram. Int.* **2020**, *46*, 24592–24604. [[CrossRef](#)]
48. Ighere, J.O.; Greaney, P.A. Characterizing Property of States: Effect of Defects on the Coefficient of Thermal Expansion and the Specific Heat Capacity of ZrB₂. *New J. Glass Ceram.* **2020**, *10*, 15–27. [[CrossRef](#)]
49. Zaouali, M.; Lebrun, J.L.; Gergaud, P. X-ray diffraction determination of texture and internal stresses in magnetron PVD molybdenum thin films. *Surf. Coat. Technol.* **1991**, *50*, 5–10. [[CrossRef](#)]
50. Liu, Z.-J.; Xing, X.-J.; Jiang, X.-Y.; Wang, X.; Zhang, L.; Jian, X.; Mu, C.-H.; Han, T.-C.; Lu, H.-P.; Zhang, L.-J.; et al. Structural self-deterioration mechanism for zirconium diboride in an inert environment. *Ceram. Int.* **2021**, in press. [[CrossRef](#)]
51. Parakhonskiy, G.; Vtech, V.; Dubrovinskaia, N.; Caracas, R.; Dubrovinsky, L. Raman spectroscopy investigation of alpha boron at elevated pressures and temperatures. *Solid State Commun.* **2013**, *154*, 34–39. [[CrossRef](#)]
52. Zhong, B.; Zhang, T.; Huang, X.X.; Wen, G.W.; Chen, J.W.; Wang, C.J.; Huang, Y.D. Fabrication and Raman scattering behavior of novel turbostratic BN thin films. *Mater. Lett.* **2015**, *151*, 130–133. [[CrossRef](#)]

53. Pokropivny, V.; Kovrygin, S.; Gubanov, V.; Lohmus, R.; Lohmus, A.; Vesi, U. Ab-initio calculation of Raman spectra of single-walled BN nanotubes. *Physica E* **2008**, *40*, 2339–2342. [[CrossRef](#)]
54. Dong, Y.; Wang, T.G.; Yan, B.; Qi, H.J.; Guo, Y.Y.; Xu, S.S. Study on the microstructure and mechanical properties of Zr-B(N) tool coatings prepared by hybrid coating system. *Procedia Manuf.* **2018**, *26*, 806–817. [[CrossRef](#)]
55. Mitterer, C.; Uebleis, A.; Ebner, R. Sputter deposition of wear resistant coatings within the system Zr-B-N. *J. Mater. Sci. Eng.* **1991**, *140*, 670–675. [[CrossRef](#)]
56. Brandstetter, E.; Mitterer, C.; Ebner, R. A transmission electron microscopy study on sputtered Zr-B and Zr-B-N films. *Thin Solid Films* **1991**, *201*, 123–135. [[CrossRef](#)]
57. Jimenez, O.; Audronis, M.; Leyland, A.; Flores, M.; Rodriguez, E.; Kanakis, K.; Matthews, A. Small grain size zirconium-Based coatings deposited by magnetron sputtering at low temperatures. *Thin Solid Films* **2015**, *591*, 149–155. [[CrossRef](#)]
58. Shtansky, D.V.; Kulinich, S.A.; Levashov, E.A.; Sheveiko, A.N.; Kiriuhanchev, F.V.; Moore, J.J. Localized Deformation of Multicomponent Thin Films. *Thin Solid Films* **2002**, *420*, 330–337. [[CrossRef](#)]
59. Leyland, A.; Matthews, A. On the significance of the H/E ratio in wear control: A nanocomposite coating approach to optimised tribological behaviour. *Wearing* **2000**, *246*, 1–11. [[CrossRef](#)]
60. Levashov, E.A.; Petrzhik, M.I.; Shtansky, D.V.; Kiryukhantsev-Korneev, F.V.; Sheveiko, A.N.; Valiev, R.Z.; Gunderov, D.V.; Prokoshkin, S.D.; Korotitskiy, A.V.; Smolin, A.Y. Nanostructured Titanium Alloys and Multicomponent Bioactive Films Mechanical Behavior at Indentation. *Mater. Sci. Eng.* **2013**, *570*, 51–62. [[CrossRef](#)]
61. Kiryukhantsev-Korneev, P.V.; Shvyndina, N.V.; Bondarev, A.; Levashov, E.A. Structure and properties of tribological coatings in Cu-B system. *Phys. Met. Metal.* **2014**, *115*, 716–722. [[CrossRef](#)]
62. Kiryukhantsev-Korneev, P.V.; Pierson, J.F.; Kuptsov, K.A.; Shtansky, D.V. Hard Cr-Al-Si-B-(N) coatings deposited by reactive and non-reactive magnetron sputtering of CrAlSiB target. *Appl. Surf. Sci.* **2014**, *314*, 104–111. [[CrossRef](#)]
63. Musil, J. Hard and superhard nanocomposite coatings. *Surf. Coat. Technol.* **2000**, *125*, 322–330. [[CrossRef](#)]
64. Okamoto, S.; Nakazono, Y.; Otsuka, K.; Shimoitani, Y.; Takada, J. Mechanical properties of WC/Co cemented carbide with larger WC grain size. *Mater. Charact.* **2005**, *55*, 281–287. [[CrossRef](#)]
65. Ürgen, M.; Çakir, A.F.; Eryilmaz, O.L.; Mitterer, C. Corrosion of zirconium boride and zirconium boron nitride coated steels. *Surf. Coat. Technol.* **1995**, *71*, 60–66. [[CrossRef](#)]
66. Srinath, A.; von Fieandt, K.; Lindblad, R.; Fritze, S.; Korvela, M.; Petersson, J.; Lewin, E.; Nyholm, L. Influence of the nitrogen content on the corrosion resistances of multicomponent AlCrNbYZrN coatings. *Corros. Sci.* **2021**, *188*, 109557. [[CrossRef](#)]
67. Hsueh, H.-T.; Shen, W.-J.; Tsai, M.-H.; Yeh, J.-W. Effect of nitrogen content and substrate bias on mechanical and corrosion properties of high-entropy films (AlCrSiTiZr)_{100-x}N_x. *Surf. Coat. Technol.* **2012**, *206*, 4106–4112. [[CrossRef](#)]
68. Mousavi, H.; Khodadadi, J.; Kurdestany, J.M.; Yarmohammadi, Z. Electrical and thermal conductivities of the graphene, boron nitride and silicon boron honeycomb monolayers. *Phys. Lett. A* **2016**, *380*, 3823–3827. [[CrossRef](#)]
69. Kameneva, A.; Kichigin, V.; Lobov, N.; Kameneva, N. Data on the effect of structure, elemental and phase composition gradient of nitride multilayer coatings on corrosion protection of different substrates in 3% NaCl and 5% NaOH solutions. *Data Brief* **2019**, *27*, 104796. [[CrossRef](#)]
70. Sharma, B.; Thapa, A.; Sarkar, A. Ab-initio study of LD-HfO₂, Al₂O₃, La₂O₃ and h-BN for application as dielectrics in MTJ memory device. *Superlattices Microstruct.* **2021**, *150*, 106753. [[CrossRef](#)]
71. Sarkarat, M.; Lanagan, M.; Ghosh, D.; Lottes, A.; Budd, K.; Rajagopalan, R. Improved thermal conductivity and AC dielectric breakdown strength of silicone rubber/BN composites. *Compos. Part C* **2020**, *2*, 100023. [[CrossRef](#)]
72. Kirk, R.E.; Othmer, D.F. *Encyclopedia of Chemical Technology*, 4th ed.; ACS Publications: Washington, DC, USA, 2001; Volume 4, p. 578.
73. Thörnberg, J.; Bakhit, B.; Palisaitis, J.; Hellgren, N.; Hultman, L.; Greczynski, G.; Persson, P.O.Å.; Petrov, I.; Rosen, J. Improved oxidation properties from a reduced B content in sputter-deposited TiB_x thin films. *Surf. Coat. Technol.* **2021**, *420*, 127353. [[CrossRef](#)]
74. Bakhit, B.; Palisaitis, J.; Thörnberg, J.; Rosen, J.; Persson, P.O.Å.; Hultman, L.; Petrov, I.; Greene, J.E.; Greczynski, G. Improving the high-temperature oxidation resistance of TiB₂ thin films by alloying with Al. *Acta Mater.* **2020**, *196*, 677–689. [[CrossRef](#)]
75. Podobeda, L.G.; Tapsuk, A.K.; Buravov, A.D. Oxidation of boron nitride under nonisothermal conditions. *Powder Metall. Met. Ceram.* **1976**, *15*, 696–698. [[CrossRef](#)]
76. Carminati, P.; Jacques, S.; Rebillat, F. Oxidation/corrosion of BN-based coatings as prospective interphases for SiC/SiC composites. *J. Eur. Ceram. Soc.* **2021**, *41*, 3120–3131. [[CrossRef](#)]